Acta Crystallographica Section A
Foundations of Crystallography
ISSN 0108-7673

Received 16 October 2000
Accepted 24 November 2000

Recovering experimental and theoretical electron densities in corundum using the multipolar model: IUCr Multipole Refinement Project

S. Pillet,[a] M. Souhassou,[a] C. Lecomte,[a]* K. Schwarz,[b] P. Blaha,[b] M. Rérat,[c] A. Lichanot[c] and P. Roversi[d]

[a]Laboratoire de Cristallographie et Modélisation des Matériaux Minéraux et Biologiques, UPRESA CNRS 7036, Faculté des Sciences, Université Henri Poincaré, Nancy I, BP 239, 54506 Vandoeuvre les Nancy, France, [b]Institute for Physical and Theoretical Chemistry, TU Vienna, A-1060 Vienna, Austria, [c]Laboratoire de Chimie Structurale, UMR CNRS 5624, Université de Pau, IFR rue Jules Ferry, F-64000 Pau, France, and [d]MRC Laboratory of Molecular Biology, Hills Road, Cambridge CB2 2QH, England. Correspondence e-mail: lecomte@lcm3b.u-nancy.fr

This electron-density study on corundum (α-Al_2O_3) is part of the Multipole Refinement Project supported by the IUCr Commission on Charge, Spin and Momentum Densities. For this purpose, eight different data sets (two experimental and six theoretical) were chosen from which the electron density was derived by multipolar refinement (using the *MOLLY* program). The two experimental data sets were collected on a conventional CAD4 and at ESRF, ID11 with a CCD detector, respectively. The theoretical data sets consist of static, dynamic, static noisy and dynamic noisy moduli of structure factors calculated at the Hartree–Fock (HF) and density functional theory (DFT) levels. Comparisons of deformation and residual densities show that the multipolar analysis works satisfactorily but also indicate some drawbacks in the refinement. Some solutions and improvements during the refinements are proposed like contraction or expansion of the inner atomic shells or increasing the order of the spherical harmonic expansion.

1. Introduction

Since the pioneering work of Coppens thirty years ago (Coppens, 1967), the study of charge densities is a mature field and hundreds of publications are devoted to inorganic and organic materials or organometallic and biomolecular crystals. With the use of 2D detectors on conventional or synchrotron X-ray diffraction facilities, more and more data are generated for electron-density studies. The data sets are mainly evaluated with multipolar atomic models (Stewart, 1969, 1979; Stewart & Spackman, 1981; Hansen & Coppens, 1978), which have become a standard tool. From these models, which express the total electron density in an analytical form, it is possible to calculate crystalline or molecular properties like charges, dipole moments, electrostatic potentials, topological parameters *etc.* It can be foreseen that soon charge-density studies will become almost routine work, in particular for small molecules and, consequently, many crystallographers will be using a multipolar refinement program, sometimes without knowing its limitations and drawbacks.

Many researchers have realised some weakness in the flexibility of the multipole refinement (see for example Epstein *et al.*, 1977; Iversen *et al.*, 1997; Coppens *et al.*, 1999; Pérès *et al.*, 1999). This observation was one of the reasons to start a multipole refinement project supported by the IUCr Commission on Charge, Spin and Momentum Densities. This paper is a first report on this project in which an inorganic and an organic crystal were selected for which both theoretical and experimental moduli of structure factors are to be determined; we want to find out to what extent the multipolar analysis can recover the real charge density from static, dynamic, noise-free or noisy diffraction data. Since some of the previous work in this context has been devoted to organic or covalent compounds [*e.g.* H_3PO_4 (Moss *et al.*, 1995; Souhassou *et al.*, 1995), urea (Zavodnik *et al.*, 1999) or intermolecular interactions (Spackman *et al.*, 1999; Coppens *et al.*, 1999; Abramov *et al.*, 1999)], this study deals with an inorganic material, namely corundum Al_2O_3, using the *MOLLY* multipole program (Hansen & Coppens, 1978), which is widely used and is now implemented in the *XD* package (Koritzansky *et al.*, 1995).

Including this *Introduction*, the present paper is divided into four parts. In §2, we describe the data sets and refinement strategies. In §3, the refinement results are discussed as well as the residual and static deformation densities and, in §4, the necessary improvements of the multipolar modelling are explained. A comparison between experimental and theoretical densities is not the topic of this paper and will be presented in a forthcoming publication.

Table 1
Crystallographic data of the corundum (α-Al_2O_3) structure in the triple hexagonal cell.

	Refinement parameters	*CRYSTAL* static starting parameters	*WIEN* static starting parameters
Space group	$R\bar{3}c$		
Unit cell	$a = b = 4.7602$ (4) Å	$a = b = 4.7602$ (4) Å	$a = b = 4.757$ (1) Å
	$c = 12.993$ (2) Å	$c = 12.993$ (2) Å	$c = 12.9877$ (1) Å
	Volume = 254.98 (5) $Å^3$		
Atomic positions	Al 12(c)		
	($00z$)	$z_{Al} = 0.35216$	$z_{Al} = 0.3522$
	O 18(e)		
	($x0\frac{1}{4}$)	$x_O = 0.30624$	$x_O = 0.3063$

2. Structure, data sets and refinement strategy

2.1. Corundum structure

Corundum, Al_2O_3, has a rhombohedral unit cell with space group $R\bar{3}c$, in which all calculations have been performed, whereas data collections and refinements were carried out in the hexagonal setting. In the latter case, the aluminium atom is at position 12(c) (threefold symmetry) and the oxygen atom is at position 18(e) (twofold symmetry). Table 1 summarizes the crystallographic parameters common to all theoretical calculations. The corundum structure is shown in Fig. 1(a) and can be described as a close packing of oxygen atoms in which the aluminium atoms are located in two thirds of the octahedral sites. Each aluminium atom is linked to six symmetry-related oxygen atoms, with two different bonding distances, 1.8551 (2) and 1.9716 (3) Å, which differ owing to the repulsion between two Al neighbours. Throughout this paper, we use the following convention: $O_1 = O^{1/3+x-y,-1/3+x,2/3-z}$, $O_2 = O^{-y,x-y,z}$, $O_3 = O^{x,y,z}$, $O_4 = O^{-x+y,-x,z}$. All density maps shown in this paper are calculated in two planes: the O_1—Al—O_2 plane and the O_2–O_3–O_4 plane perpendicular to the c axis. The first plane contains the two Al—O bonds, the short one and the long one, respectively Al—O_1 and Al—O_2 (Fig. 1a). The latter plane contains a common face of two linked Al octahedra, point C being the centre of this face.

2.2. Data sets

Eight data sets have been selected, two of which being experimental data. They are described in Table 2. The experimental data are those of Lewis *et al.* (1982), labeled LSF, collected on a CAD4 diffractometer at room temperature with Ag $K\alpha$ radiation and those of Graafsma *et al.* (1998), hereafter denoted GS, collected at ESRF ID11 with a Siemens Smart CCD detector at high energy, $E = 60$ keV ($\lambda = 0.2145$ Å), and at 120 K. The LSF data were carefully corrected for absorption and anomalous-dispersion effects; secondary extinction has been refined (see later). The GS data were not corrected for absorption owing to the high energy of the incident radiation. The reader is referred to the original papers for more details on data reduction. Among the many experimental data sets available (Kirfel & Eichhorn, 1990; Brown *et al.* 1993; Maslen *et al.*, 1993; Lewis *et al.*, 1982; Graafsma *et al.*, 1998), the two latter data sets were chosen because corundum suffers very much from extinction, which in the selected experimental data is the smallest (these data were collected at the shortest wavelengths: LSF, Ag $K\alpha$ radiation; GS, $\lambda = 0.2145$ Å). These two experimental data sets served to test whether the multipolar model is flexible enough to accurately fit actual experimental data and to produce a valid (*i.e.* positive) electron density even in low-density regions.

We made two different types of *ab initio* calculation, one based on density functional theory (DFT) using the *WIEN97* code (Blaha, Schwarz & Luitz, 1997; Blaha, Schwarz, Sorantin & Trickey, 1997) and one based on Hartree–Fock (HF) theory and the *CRYSTAL95* program (Dovesi *et al.*, 1996). These calculations led to two sets of static moduli of structure factors denoted as WS and CS, respectively. The DFT (*WIEN97*)

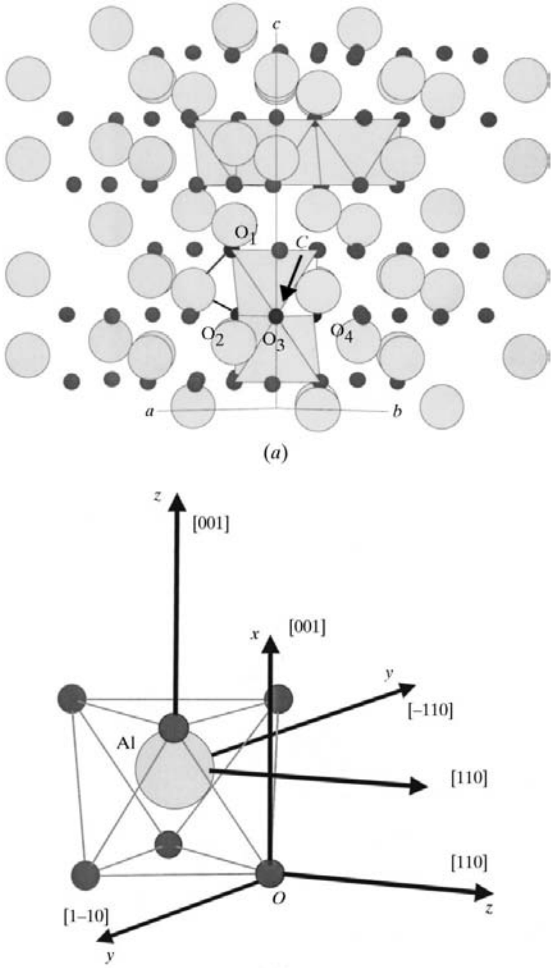

(a)

(b)

Figure 1
(a) Structure of corundum in the hexagonal cell, viewed along the a+b (or [11$\bar{2}$0]) direction. Grey circles are aluminium atoms and black ones are oxygen. A few Al octahedra are represented. Point C is the centre of the common face between two Al octahedra. (b) Local atomic coordinate axes used in the refinements (hexagonal setting).

Table 2
Characteristics of the different data sets.

Data set		$\sin\theta/\lambda\|_{\max}$ (Å^{-1})	No. of unique reflections	Thermal smearing	Noise	Obtained from
WIEN static	WS	1.898	1632	–	–	*WIEN97*
WIEN dynamic	WD	1.898	1632	Isotropic	–	*WIEN97*
WIEN static noisy	WSN	1.898	1632	–	Gaussian	*WIEN97*
WIEN dynamic noisy	WDN	1.898	1632	Isotropic	Gaussian	*WIEN97*
CRYSTAL static	CS	1.898	1632	–	–	*CRYSTAL95*
CRYSTAL dynamic	CD	1.898	1632	Anisotropic	–	*CRYSTAL95*
Lewis *et al.* (1982)	LSF	1.495	804	Experiment	Experiment	CAD4 data (Ag $K\alpha$)
Graafsma *et al.* (1998)	GS	1.25	432	Experiment	Experiment	ESRF synchrotron data, 120 K (λ = 0.2145 Å)

Table 3
Effect of Gaussian noise on a few reflections [$|F_{\rm noisy}|^2 = |F_W|^2 + {\rm Gauss} \times \sigma(|F_W|^2)$] for WS data.

(hkl)	(006)	(0,0,12)	(024)	(036)	(104)	(1,0,10)	(116)	(1,2,14)
$\|F_W\|$	5.932	18.764	31.491	4.471	27.262	28.269	35.084	17.071
$\|F_{\rm noisy}\|$	6.103	18.573	31.384	4.471	27.357	28.408	34.572	17.114
$\sigma(\|F_W\|)$	0.069	0.130	0.268	0.068	0.210	0.222	0.329	0.117
$(\|F_{\rm noisy}\| - \|F_W\|)/\sigma(\|F_W\|)$	2.48	−1.47	−0.40	0	0.45	0.62	−1.55	0.37

calculations used the generalized gradient approximation (GGA) (Perdew *et al.*, 1996, 1997) and employed the linearized augmented plane wave (LAPW) method. The starting position parameters were $z_{\rm Al} = 0.3522$ and $x_{\rm O} = 0.3063$. The HF (*CRYSTAL95*) computation used the linear combination of atomic orbitals (LCAO) method where the AO basis sets describing aluminium and oxygen were those reported by Salasco *et al.* (1991), including one additional polarization function on both atoms (aluminium exponent = 0.38 and oxygen exponent = 0.80). It is noted that the use of these functions decreases slightly the ionic character of corundum. The starting position parameters were $z_{\rm Al} = 0.35216$ and $x_{\rm O} = 0.30624$. Both WS and CS moduli of structure factors were calculated with appropriate displacement parameters in order to check whether a known charge density can be recovered with the multipole refinement scheme by deconvoluting thermal motion. Since the WS data are not derived from an atomic-site-centred basis but from plane waves, it is not possible to assign unambiguously different temperature parameters to the two atomic sites, thus, one general isotropic term ($U_{\rm iso}$ = 0.00335 Å^2) was applied to the WS data,

$$|F_{\rm WD}| = |F_{\rm WS}| \exp(-8\pi^2 U_{\rm iso} \sin^2\theta/\lambda^2), \qquad (1)$$

in order to generate a new set of dynamic moduli of structure factors labelled WD. This is of course a crude approximation to simulate real atomic vibrations but it is a clearly defined model to judge whether the multipole model is able to recover static densities from finite temperature data.

The dynamic HF–LCAO moduli of structure factors were derived according to the method of Azavant *et al.* (1994, 1996), with the use of experimental anisotropic displacement parameters of Al and O reported by Lewis *et al.* (1982) [for Al: U^{11} = 0.00279 (3), U^{33} = 0.00296 (3) Å^2; for O: U^{11} = 0.00327 (3), U^{22} = 0.00341 (3), U^{33} = 0.00365 (3), U^{13} = 0.00047 (2) Å^2]. These data are called CD. This way of generating anisotropic thermal smearing affects each modulus of the structure factors separately, whereas, in the WD data, reflections with the same scattering angle are affected by the same Debye–Waller factor.

Finally, to simulate more closely the X-ray experiments, we also generated two sets of noisy data (WSN and WDN), derived from the *WIEN* structure factors in the following way (see Appendix *A*):

$$|F_{\rm noisy}|^2 = |F_W|^2 + {\rm Gauss} \times \sigma(|F_W|^2), \qquad (2)$$

where F_W refers to static (WS) or dynamic (WD) data. $\sigma(|F_W|^2)$ were calculated from the LSF experimental data; Gauss is a random deviate of unit variance. As reported in Appendix *A*, this noise simulation may not be appropriate for very weak reflections, *i.e.* mainly for the highest-angle parts of the data sets. However, owing to the resolution cut-off used, by which most of these weak reflections are not included in the refinements, this has no significant influence (as tested) on the refinement results. Table 3 shows how much some moduli of structure factors are affected by noise. As shown in Table 2, all theoretical moduli of structure factors were calculated up to a resolution of $\sin\theta/\lambda$ = 1.898 Å^{-1}, whereas the resolution of the experimental data, LSF and GS, is 1.495 and 1.25 Å^{-1}, respectively.

2.3. Refinement strategy

The Hansen–Coppens model (program *MOLLY*: Hansen & Coppens, 1978) was used and refined against all data sets. In this model, the electron density is described as

$$\rho(\mathbf{r}) = \rho_{\rm core}(r) + P_v\kappa^3\rho_{\rm val}(\kappa r) + \sum_{l=0}^{l_{\max}} \kappa'^3 R_l(\kappa' r) \sum_{m=0}^{+1} \sum_p P_{lmp} y_{lmp}(\theta, \varphi), \qquad (3)$$

where the first two terms $\rho_{\rm core}$ and $\rho_{\rm val}$ are the spherically averaged core- and valence-electron densities of the free atom; the corresponding core and valence scattering factors were calculated from atomic wave functions (Clementi & Roetti, 1974). The last term is the expansion of the valence density on the y_{lmp} spherical harmonic functions in real form. All refinements, as will be discussed later, were performed with a new version of *MOLLY* (Souhassou *et al.*, 1999), which includes multipoles up to $l = 6$. The refineable parameters P_v and P_{lmp} are the valence and multipole populations, respectively, whereas κ and κ' allow, for each atom, the valence densities to contract or expand owing to bonding interactions (Coppens *et al.*, 1979). Radial functions are chosen as Slater-type functions with a different radial function for each multipole order l:

$$R_l(r) = [\zeta^{n_1+3}/(n_1+2)!]r^{n_1}\exp(-\zeta r). \qquad (4)$$

The parameters that define each radial function are n_l and ζ. First tests concerning the Al and O radial functions were performed and the resulting n_l and ζ (bohr^{-1}) parameters are given in Table 4(*a*). The Slater-type radial functions are given in Figs. 2(*a*) and 2(*c*) together with the Al and O valence scattering factors (Figs. 2*b* and 2*d*). While the Slater-type functions used for the O atoms are contracted with maxima at less than 0.5 Å from the nucleus, the aluminium ones are more diffuse and their maxima and widths increase with the multipole order. These diffuse functions are necessary to describe the density far from the atoms. All results described in §3 had $l_{\max} = 4$ for both Al and O. The necessity to use higher l order ($l > 4$) is discussed in §4. The local coordinate axes were chosen according to the three- and twofold symmetries of the Al and the O atoms, respectively (Fig. 1*b*).

Table 4(*b*) gives the refinement procedure used for all theoretical and experimental data. The 1.2 Å^{-1} $\sin\theta/\lambda$ cut-off was chosen in order to be close to the resolution of a usual

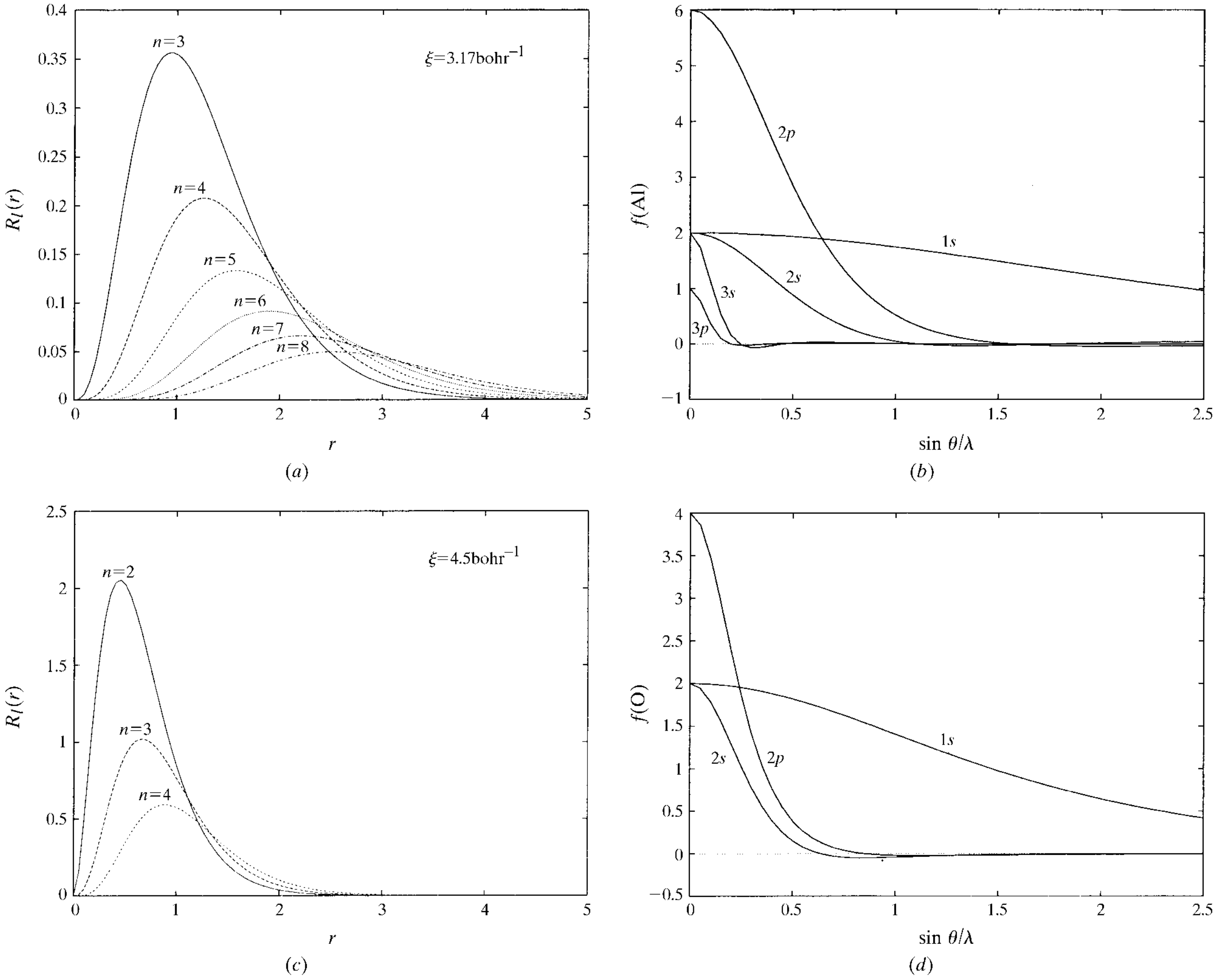

(*a*) (*b*)

(*c*) (*d*)

Figure 2

(*a*) Aluminium and (*c*) oxygen radial functions $R_l(r)$ *versus* distance r (bohr) and (*b*), (*d*) the corresponding scattering factors (in electrons) *versus* $\sin\theta/\lambda$ (Å^{-1}) .

$X - X$ experiment and the 0.8 Å^{-1} $\sin\theta/\lambda$ threshold is the limit beyond which the valence scattering factors have very small contributions (Figs. 2*b*, *d*). The presented refinements were based on $|F|$ with the full-matrix method and all reflections were included with $|F| > 3\sigma(|F|)$ for noisy and experimental data sets. After a refinement of the scale factor with all data, atomic positions and appropriate thermal parameters, if any (isotropic or anisotropic), were refined using high-order ($0.8 < \sin\theta/\lambda < 1.2$ Å^{-1}) data (spherical-atom model).

In the second stage, the valence density parameters (P_v, κ, P_{lmp} and κ') were refined separately until convergence was achieved at low angles ($\sin\theta/\lambda < 0.8$ Å^{-1}). To analyse the fitting procedure and the results of the multipolar model, we can define a residual density by

$$\Delta\rho_{\rm resid}(\mathbf{r}) = V^{-1}\sum_{\mathbf{H}}[k^{-1}|F_{\rm obs}(\mathbf{H})| - |F_{\rm mult}(\mathbf{H})|]\exp(i\Phi_{\rm mult}) \times \exp(-2i\pi\mathbf{H}\cdot\mathbf{r}), \qquad (5)$$

where $|F_{\rm obs}|$ is the observed (or reference) modulus of the structure factor and $|F_{\rm mult}|\exp(i\Phi_{\rm mult})$ is calculated from the multipolar refinement. $\mathbf{H}$ is the scattering vector and k is the refined scale factor. Since large residues appeared in the core regions of the residual map (Fig. 4*a*) calculated with all data in the first test refinements of WS data, an Al core contraction parameter [as defined in (6)] was refined using high-order data ($\sin\theta/\lambda > 0.8$ Å^{-1}). With this formalism, the core scattering factor for aluminium is given by

$$f_{\rm core}(H) = 2f_{1s}(H) + 8f_{2s,2p}(H/\kappa_{L\text{-Al}}). \qquad (6)$$

In fact, $\kappa_{L\text{-Al}}$ provides a rescaling of the Al core scattering factor used in the refinements. It is well known that DFT core wave functions are slightly more expanded than HF wave functions, and that HF is usually better for those core states (see for example Zuo *et al.*, 1997). In this paper, we tried to fit a DFT core with a HF core (Clementi wave functions) and a core κ parameter was needed to account for the difference.

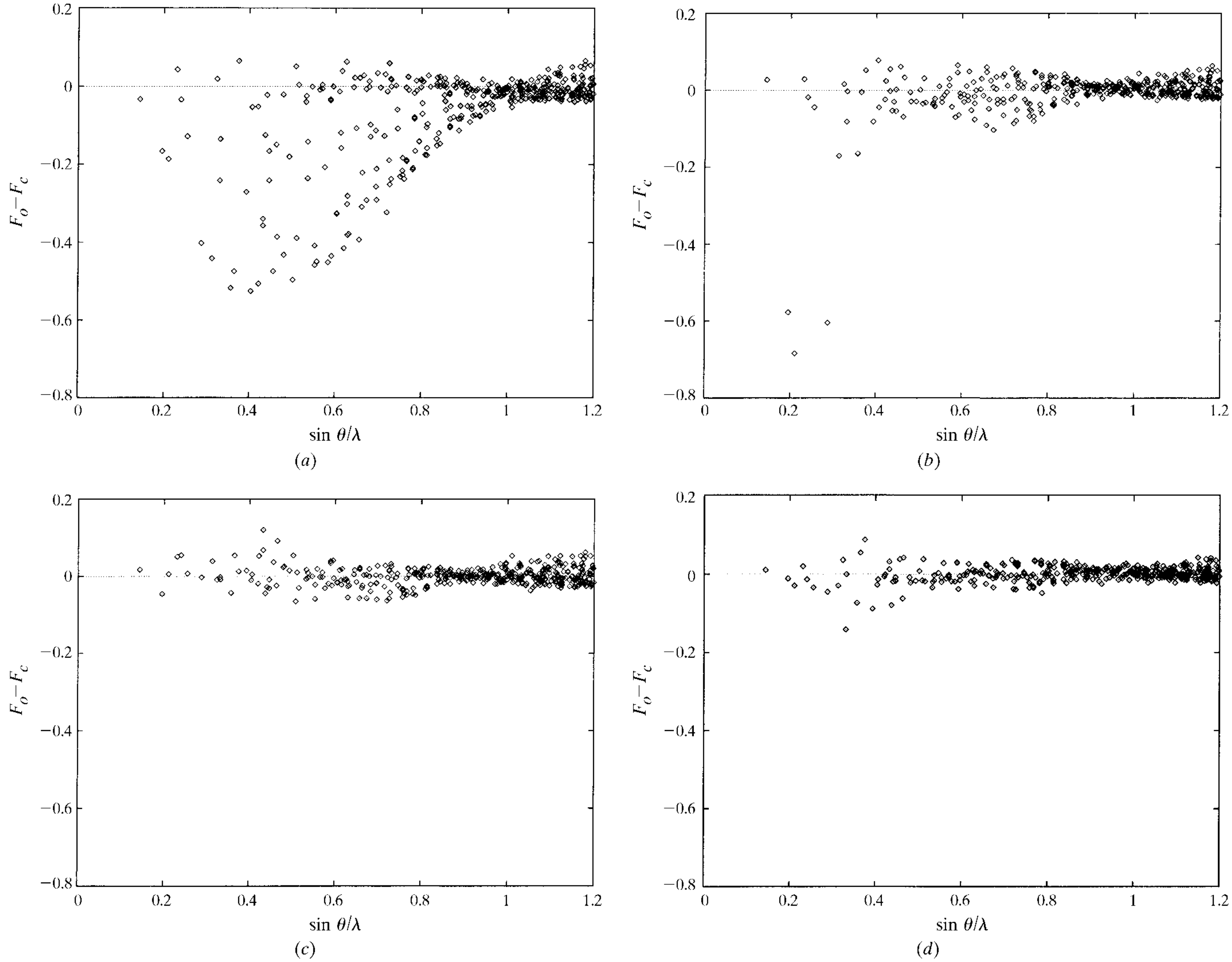

(*a*) (*b*) (*c*) (*d*)

Figure 3

Difference (in electrons) between observed and calculated structure-factor amplitudes *versus* $\sin\theta/\lambda$ (Å^{-1}): (*a*) WS data without $\kappa_{L\text{-Al}}$ core refinement ($l_{\rm max} = 4$); (*b*) WS data after $\kappa_{L\text{-Al}}$ core refinement ($l_{\rm max} = 4$); (*c*) CS data, after $\kappa_{L\text{-Al}}$ core refinement ($l_{\rm max} = 4$); (*d*) same as (*b*) but with $l_{\rm max} = 6$ for Al atoms.

Table 4
Radial function parameters and refinement strategy.

(*a*) Radial function parameters

	l	1	2	3	4	5	6
Al	n_l	3	4	5	6	7	8
	ξ (bohr^{-1})	3.17	3.17	3.17	3.17	3.17	3.17
O	n_l	2	2	3	4	–	–
	ξ (bohr^{-1})	4.5	4.5	4.5	4.5	–	–

(*b*) Refinement strategy

High order 0.8 Å^{-1} < $\sin\theta/\lambda$	Low order $0 < \sin\theta/\lambda < 0.8$ Å^{-1}	All data $0 < \sin\theta/\lambda < 1.2$ Å^{-1}
(1) x, y, z U^{ij} $\kappa_{L\text{–Al}}$	(2) P_v P_{lmp} κ κ' Separately: P_v and κ P_{lmp} and κ'	(3) All parameters

Surprisingly, a refinement of this parameter improved the results based on the HF static (CS) data, a similar improvement is also observed for both experimental data.

Finally, an all-data refinement up to the experimental resolution (1.2 Å^{-1}) was performed over all parameters, except the valence κ' parameter, which was kept fixed because of large correlations. At this stage, damping was required on the contraction-expansion parameters, κ and κ', in order to achieve a good convergence of the model [for a discussion on the κ' refinement, see Pérès *et al.* (1999)]. For the two sets of experimental data, the isotropic extinction was refined; this has led to an insignificant value for the GS data but to a maximum extinction of 24% (reflection 300) for the LSF data, using the Becker–Coppens model (Becker & Coppens, 1974, 1975) type I with a Lorentzian distribution, in close agreement with the results of Lewis *et al.* (1982) (24% for reflection 300).

3. Refinement results, discussion of the residual and deformation densities

3.1. Statistical parameters

Whatever the data set, at convergence, all statistical agreement indices are excellent as shown in Table 5. All agreement indices given in this table were calculated with the maximum limit in resolution common to all data sets, that is $\sin\theta/\lambda < 1.2$ Å^{-1} and using all reflections. The density maps presented in other sections were also calculated with this limit, which enables direct and consistent comparisons between all the different results. The best fit is obtained for the static (CS) and dynamic (CD) Hartree–Fock data. The fit is slightly poorer for the DFT calculation owing to the limited order of the angular functions in the refinement of the aluminium charge density ($l_{\max} = 4$), but improves when one allows $l_{\max} = 6$ in the multipolar refinement. Therefore, from a statistical point of view, the multipolar model used works satisfactorily for all simulated or experimental data with good GOF values for noisy and experimental data sets.

Table 5
Summary of the agreement factors (calculated on $|F|$, with $\sin\theta/\lambda \leq 1.2$ Å^{-1}).

Data set	$l_{\max}$	R (%)	R_W (%)	GOF	No. of unique reflections
WS ($\kappa_{L\text{–Al}} = 1$)	4	0.77	0.71		413
WS ($\kappa_{L\text{–Al}}$ refined)	4	0.39	0.68		413
WS ($\kappa_{L\text{–Al}}$ refined)	6	0.27	0.27		413
CS ($\kappa_{L\text{–Al}} = 1$)	4	0.41	0.45		413
CS ($\kappa_{L\text{–Al}}$ refined)	4	0.21	0.22		413
WSN	4	1.46	1.24	1.08	413
WD	4	0.40	0.57		413
CD	4	0.20	0.29		413
WDN	4	1.36	1.23	1.08	413
LSF	4	1.65	0.89	1.66	413
GS	4	1.39	1.78	1.58	409

3.2. Residual density

The analysis of the residual electron densities may be performed in reciprocal space by analysing $|F_o| - |F_c|$ *versus* $\sin\theta/\lambda$ and in direct space by directly analysing the residual density [equation (5)] maps.

First, in reciprocal space, inspection of Fig. 3(*a*) shows that the standard multipolar model does not work so well in reproducing the WS data. It was necessary to allow for substantial core contraction on the Al site with a $\kappa_{L\text{–Al}}$ parameter (Fig. 3*b*). Once this $\kappa_{L\text{–Al}}$ parameter is used, the multipole model works quite well as shown by Figs. 3(*b*) and 3(*c*) (WS and CS, respectively), only three low-resolution WS structure amplitudes disagree. To fit these three reflections satisfactorily, higher multipole moments ($l_{\max} = 6$) had to be introduced (Fig. 3*d*). Both of these improvements to the multipolar model will be discussed in more detail in §4.

In real space, we discuss the residual densities (Fig. 4) calculated from WS, WSN, CS, GS and LSF data; the remaining maps are given as supplementary material.[1]

Also in real space it is clear that a $\kappa_{L\text{–Al}}$ refinement is necessary to reduce the residual density (Figs. 4*a* and 4*b*). The CS residual map (Fig. 4*c*) is the cleanest one with a maximum residual density of 0.02 e Å^{-3} close to the O atom and only one contour (0.01 e Å^{-3}) in the bonding region. The WS residual map (Fig. 4*b*) has more residues, especially close to the Al nucleus where the negative density reaches −0.1 e Å^{-3}; the Al—O bonding density is also slightly less well reproduced than for the Hartree–Fock data. As expected, this negative residual density found in WS does not show up clearly in the WSN data (Fig. 4*d*) because of the noise. The experimental residual maps are plotted with a contour level five times greater than for the theoretical data. The modelled experimental noise then appears to be lower than the experimental one. Residual LSF maps are cleaner than for GS data. For these latter data, large residues close to aluminium atoms show up, which could not be accounted for in the model; all attempts to model these features were unsuccessful. Other

---

[1] Residual density and static deformation maps not shown in Figs. 4, 5 and 6 are available from the IUCr electronic archives (Reference: SH0148). Services for accessing these data are described at the back of the journal.

residual maps, given in the supplementary material, do not give important new information.

3.3. Structural and model parameters

From a geometrical point of view, atomic positions and thermal smearing parameters are summarized in Table 6. As mentioned above, *WIEN* and *CRYSTAL* calculations were performed with the same starting parameters (Table 1). After multipole refinement, the Al and O positions remain within the estimated uncertainties at the starting parameters, varying from $z_{\rm Al}$ = 0.352194 (4) to $z_{\rm Al}$ = 0.352205 (6) and $x_{\rm O}$ = 0.306284 (7) to $x_{\rm O}$ = 0.30634 (7) for all *WIEN* results [from $z_{\rm Al}$ = 0.352165 (4) to $z_{\rm Al}$ = 0.352167 (3) and from $x_{\rm O}$ = 0.306258 (8) to $x_{\rm O}$ = 0.306260 (5) for *CRYSTAL* data]. For both types of calculation (static, dynamic, noise-free and noisy), these positions are in excellent agreement with the starting ones. This result clearly demonstrates that the positions obtained by multipole refinement are not biased by the presence of noise or thermal smearing.

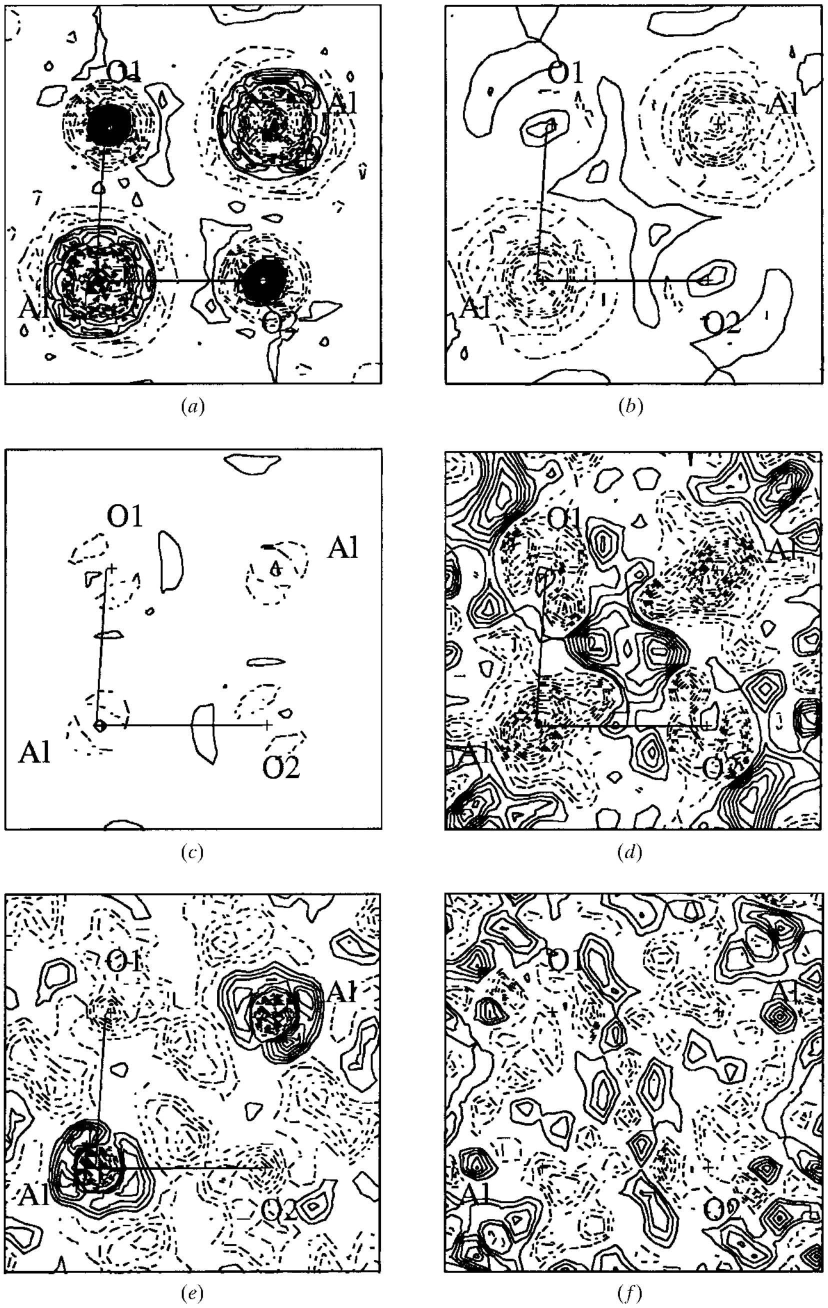

(*a*) (*b*) (*c*) (*d*) (*e*) (*f*)

Figure 4
Residual density in the O_1-Al-O_2 plane: (*a*) WS data without $\kappa_{L-{\rm Al}}$ core refinement for Al; all other plots (*b*)–(*f*) are after $\kappa_{L-{\rm Al}}$ core refinement for Al; (*b*) WS data; (*c*) CS data; (*d*) WSN data; (*e*) GS data; (*f*) LSF data. Contours are plotted at 0.01 e Å^{-3} (0.05 e Å^{-3} for GS and LSF data), negative contours dashed, zero contour omitted.

Concerning the WD and WDN data, the following isotropic thermal parameters $U_{\rm iso}$ were found after the multipole refinement: 0.003170 (9) and 0.00328 (2) Å^2, respectively, for Al, and 0.003209 (4) and 0.00329 (2) Å^2, respectively, for O, which should be compared with the $U_{\rm iso}$ = 0.00335 Å^2 value that was used to simulate the thermal effects. For both atoms, aluminium and oxygen, the $U_{\rm iso}$ parameters differ by more than 20 s.u.'s [$\Delta U_{\rm iso}/\sigma(U_{\rm iso})$ = 20 for aluminium and 35 for oxygen] when derived from the noise-free data; this discrepancy is much smaller for those derived from noisy data [$\Delta U_{\rm iso}/\sigma(U_{\rm iso})$ = 3.5 for aluminium and 3 for oxygen, but $\sigma(U_{\rm iso})$ is larger], although the scale factor k is closer to the expected $k = 1/3$ for WD than for WDN data. As the U parameters are mainly derived from the core electrons, this is certainly a consequence of the core-electron basis functions used in DFT calculations. The atomic displacement parameters obtained from refinement of the CD data are in much closer agreement with those introduced in the calculation of this data set: [for Al: U^{11} = 0.00279 (3), U^{33} = 0.00296 (3) Å^2; for O: U^{11} = 0.00327 (3), U^{22} = 0.00341 (3), U^{33} = 0.00365 (3), U^{13} = 0.00047 (2) Å^2]. The maximum discrepancy is 4 s.u.'s for U^{33}(Al).

The valence population P_v of Al is smaller than its formal value for all data sets, varying from 2.136 (9) to 2.808 (2) for the *WIEN* data and 2.025 (2) to 2.598 (2) for the *CRYSTAL* data sets [2.81 (1) and 2.23 (2) for LSF and GS experimental data, respectively]. The oxygen atom varies in the opposite way in order to satisfy the electroneutrality constraint. The fits to the dynamic data sets always lead to a lower P_v for Al than for the static data and this effect is much larger than the difference between DFT and HF data sets. This seems to be a systematic feature that is correlated to the thermal smearing: P_v(Al) has the lowest value for the WD, WDN and CD data sets compared with the results obtained for WS, WSN and CS. We also note that the valence κ parameter of aluminium is also not well determined, being positively correlated with P_v(Al), contrary to that of oxygen which is stable and nearly 0.98, in good agreement with the paper of Pérès *et al.* (1999). The reason for this becomes obvious by looking at Figs. 2(*b*) and 2(*d*), where one can see that the valence scattering factor for Al 3*s* and 3*p* (free-atom approximation) practically vanishes for $\sin\theta/\lambda > 0.25$ Å^{-1}, whereas the O 2*p* scattering factor reaches up to 1 Å^{-1}; thus, only very few reflections determine the actual Al valence population. Consequently, the net atomic charge and the κ parameters for Al atoms cannot be accurately determined from the multipole refinement. This observation holds also for Si and P atoms (as discussed in Pérès *et al.*, 1999).

3.4. Deformation density

The most important questions when refining electron densities with a model (here the multipolar Hansen–Coppens model) are: (i) can a given model recover the original electron density?; and (ii) does it accurately deconvolute thermal smearing and noise from the valence density? In order to answer these questions, the deformation densities for *WIEN* (Figs. 5 and 6) and *CRYSTAL* (Figs. 7 and 8) data have been calculated in the $O_1—Al—O_2$ and $O_2—O_3—O_4$ planes, respectively. The first figures (Figs. 5*a*, 6*a*, 7*a*, 8*a*) always display the calculated deformation densities directly obtained from *WIEN* and *CRYSTAL* calculations, respectively. They are calculated in direct space as the difference $\rho_{Al_2O_3} - \rho_{\rm atoms}^{\rm superposed}$ and do not suffer from any series truncations or model parameters and thus score as 'benchmarks' for the refined static model deformation densities. The corresponding static deformation densities obtained from the experimental GS and LSF data sets are given in Fig. 9. These represent the densities one derives from accurate experimental data, which include the combined effects of noise, thermal smearing and systematic errors. To remove these effects, a model may introduce a bias during refinements, which is the subject of this discussion.

The directly calculated static deformation densities obtained from the *WIEN* calculation in the $O_1—Al—O_2$ plane (Fig. 5*a*) shows, as expected, a positive density around O and a slightly negative density around Al owing to the higher electronegativity of the oxygen atoms. The O deformation density has peaks along the O—Al direction with heights of 0.3 and 0.25 e Å^{-3} for the short and long bonds, respectively. In the *WIEN* model densities (Figs. 5*b*, 5*c*, 5*d*), the main features of this map are recovered. The positions of the maxima along the two Al—O bonds remain the same but, for the dynamic data sets (WD, WDN), we observe an increase by 0.05 to 0.1 e Å^{-3} in peak heights in both the short and the long bonds. In that case, the multipolar model overestimates the electron density in the bonding regions (+0.1 e Å^{-3}), but the diffuse negative densities far from the nuclei are well described. This increase of electron density by the refinement compared to the 'benchmark' density (Fig. 5*a*) is correlated with the increase in the valence population (P_v) for the oxygen atom mentioned above, observed from WS to WD and from WSN to WDN data: a greater P_v for the O atom means more electron density isotropically distributed around this atom. On the other hand, by comparing the deformation densities obtained from noise-free and noisy data, we see that the electron density is almost not altered by noise (Fig. 5*d*), indicating that the noise was properly filtered by the multipolar fit. A slight change in the density shape occurs.

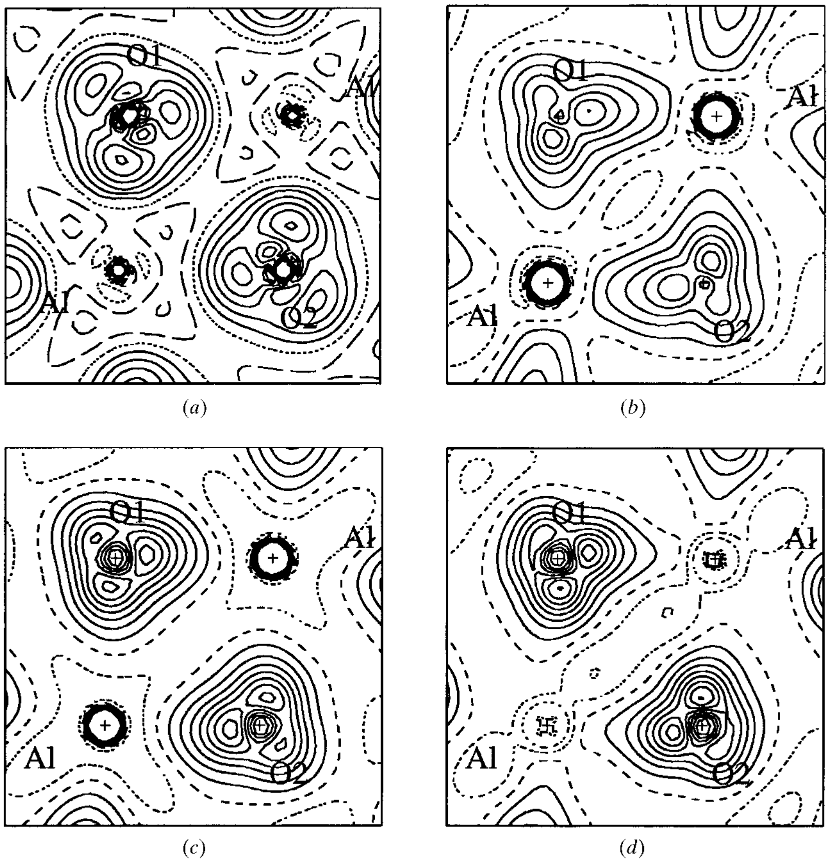

(*a*) (*b*) (*c*) (*d*)

Figure 5
Static deformation density in the $O_1—Al—O_2$ plane passing through two Al and two O atoms and showing the two different Al—O bonds: (*a*) Directly calculated from *WIEN97*; (*b*) obtained from *MOLLY* refinement ($l_{\max} = 4$) with WS data; (*c*) obtained from *MOLLY* refinement ($l_{\max} = 4$) with WD data; (*d*) obtained from *MOLLY* refinement ($l_{\max} = 4$) with WDN data. Contours are plotted at 0.05 e Å^{-3} intervals, zero contour dotted, negative dashed.

In the plane of the three oxygen atoms (Fig. 6*a*), the theoretical benchmark deformation density shows three lobes (0.20–0.25 e Å^{-3}) directed towards the centre of the octahedron face (*C*), where the deformation density is slightly negative −0.05 e Å^{-3}. The multipole model gives the same features but with an increase of electron density of 0.1 e Å^{-3} (Fig. 6*b* and supplementary material). Additional

Table 6
Summary of the refined parameters for all the data sets; κ, κ', P_v are defined in equation (3).

k is the scale factor and $U_{\rm iso}$, U^{11}, U^{33}, U^{13} are thermal displacement parameters (Å^2) defined as $T(H) = \exp\left(-2\pi^2 \sum_{i,j} h_i h_j a_i^* a_j^* U^{ij}\right)$.

Data set		WS ($l_{\rm max}$ = 4)	WS ($l_{\rm max}$ = 6)	WD	WSN	WDN
	k	0.3340 (1)	0.33452 (5)	0.3324 (7)	0.3339 (2)	0.3360 (2)
Al	$\kappa_{\rm Al}$	1.059 (3)	1.084 (4)	0.998 (5)	1.012 (8)	1.02 (1)
	$\kappa'_{\rm Al}$	1.065 (9)	1.055 (8)	1.10 (2)	1.04 (2)	1.29 (5)
	$\kappa_{L{\rm -Al}}$	1.0058 (2)	1.0034 (2)	1.0071 (2)	1.0070 (3)	1.0004 (4)
	$z_{\rm Al}$	0.352198 (9)	0.352194 (4)	0.352205 (6)	0.35220 (1)	0.35220 (1)
	$U_{\rm iso}$	–	–	0.003170 (9)	–	0.00328 (2)
	U^{11}	–	–	–	–	–
	U^{33}	–	–	–	–	–
	P_v	2.652 (5)	2.808 (2)	2.217 (3)	2.466 (9)	2.136 (9)
O	$\kappa_{\rm O}$	0.9942 (4)	0.9973 (4)	0.9804 (6)	0.9907 (7)	0.978 (1)
	$\kappa'_{\rm O}$	1.17 (4)	1.17 (3)	1.11 (5)	0.93 (4)	1.06 (7)
	$x_{\rm O}$	0.30631 (2)	0.306284 (7)	0.30631 (1)	0.30631 (2)	0.30634 (7)
	$U_{\rm iso}$	–	–	0.003209 (4)	–	0.00329 (2)
	U^{11}	–	–	–	–	–
	U^{33}	–	–	–	–	–
	U^{13}	–	–	–	–	–
	P_v	6.232 (5)	6.128 (2)	6.522 (3)	6.356 (9)	6.576 (9)

Data set		CS	CD	LSF	GS
	k	0.33170 (8)	0.33293 (5)	1.0091 (4)	0.9452 (8)
Al	$\kappa_{\rm Al}$	0.867 (3)	0.898 (2)	1.02 (1)	1.11 (3)
	$\kappa'_{\rm Al}$	0.931 (6)	1.067 (4)	1.02 (1)	1.04 (3)
	$\kappa_{L{\rm -Al}}$	1.0107 (1)	1.00593 (7)	1.0024 (5)	1.0099 (7)
	$z_{\rm Al}$	0.352167 (3)	0.352165 (4)	0.35217 (2)	0.352100 (9)
	$U_{\rm iso}$	–	–	–	–
	U^{11}	–	0.00272 (9)	0.00255 (3)	0.00117 (3)
	U^{33}	–	0.00292 (1)	0.00266 (4)	0.00146 (4)
	P_v	2.598 (2)	2.025 (2)	2.81 (1)	2.23 (2)
O	$\kappa_{\rm O}$	0.9859 (3)	0.9563 (2)	0.988 (1)	0.972 (2)
	$\kappa'_{\rm O}$	1.23 (3)	0.84 (1)	0.96 (6)	0.85 (7)
	$x_{\rm O}$	0.306260 (5)	0.306258 (8)	0.30634 (2)	0.30626 (2)
	$U_{\rm iso}$	–	–	–	–
	U^{11}	–	0.003293 (8)	0.00305 (3)	0.00168 (1)
	U^{33}	–	0.003645 (2)	0.00350 (5)	0.00208 (3)
	U^{13}	–	0.000163 (3)	0.00034 (2)	0.000217 (1)
	P_v	6.268 (2)	6.650 (2)	6.14 (1)	6.51 (2)

tests have shown that higher-order multipoles do not introduce any change in the shape of the deformation densities or in the height of the peaks (+0.01 e Å^{-3} around O, −0.05 e Å^{-3} in the vicinity of Al, see below).

The conclusions we can draw from the map derived from the HF–*CRYSTAL* data are similar. However, in the benchmark HF map (Fig. 7*a*), the negative deformation density around the Al atoms is much more pronounced, a feature that is not reproduced in the CS static deformation density. This is due to the spherical neutral atoms reference state, which is subtracted from the total model density to generate the deformation density. This spherical-atom reference state is different for the Al atom in the *CRYSTAL* map (Fig. 7*a*) (Dovesi *et al.*, 1996) from that used to generate the CS and CD maps. Similarly, in the $O_2-O_3-O_4$ plane, the negative features ('holes') at *C* are not reproduced by the multipolar model maps (Figs. 8*a*, *b*).

The static deformation densities obtained from the experimental data sets (Fig. 9) agree qualitatively between each other. Quantitatively, the maxima of the density in the Al—O bonds differ by 0.1 e Å^{-3}, and the bond polarization and general shape deviate for the two sets. These differences between the two experimental data sets are more pronounced than those between static and dynamic data, noise-free and noisy data.

From these results, we conclude that the static model is only weakly affected by noise or thermal smearing, since the multipolar models managed to extract from all data sets (static plus thermal smearing and/or noise) the most important features of the electron density, namely the positive but deformed O density.

4. Improvement of the standard multipolar model

As mentioned above, core expansion/contraction is required for some data sets. Among the four refinements that led to a core $\kappa_{L{\rm -Al}}$ parameter for aluminium greater than one (Table 6), the three *WIEN* data sets (WS, WD, WSN) show an average of $\langle\kappa_{L{\rm -Al}}\rangle = 1.0066$. Fig. 3 illustrates the discrepancies between observed and calculated structure factors *versus* $\sin\theta/\lambda$. Without the refinement of the core $\kappa_{L{\rm -Al}}$ parameter, most low-order structure-factor amplitudes $k^{-1}|F_{\rm obs}|$ are smaller than $|F_{\rm mult}|$ (Fig. 3*a*). These differences between observed and calculated moduli of structure factors decrease when we introduce a core $\kappa_{L{\rm -Al}}$ parameter in the refinements (Fig. 3*b*); upon refinement of $\kappa_{L{\rm -Al}}$, the agreement factor *R* decreases from 0.77 to 0.39% for WS and from 0.41 to 0.20% for CS, for which $\kappa_{L{\rm -Al}}$ was 1.0107 (1) (Table 5). Although it is theoretically justified to introduce $\kappa_{L{\rm -Al}}$ for the WS data, it is less well understood for CS for which a similar improvement was noted above (end of §2.3). The $\kappa_{L{\rm -Al}}$ parameter for the GS data set is also large [1.0099 (7)].

Furthermore, while most reflections are very well fitted by the multipolar model, a few (low-resolution) strong reflections (most of which would be affected by extinction if experimental data) show large differences (see Table 7) and seem to be overestimated by the multipolar model. This phenomenon appears only for experimental and *WIEN* data. For example, in the refinement of the experimental GS data, a *negative total*

Table 7
Largest discrepancies between observed and calculated structure-factor amplitudes for a few reflections on an absolute scale.

Extinction factors Y are defined as $F_{\rm corr}(\mathbf{H}) = |F_{\rm obs}(\mathbf{H})|/Y$ (Becker & Coppens, 1974, 1975).

(*a*) $|F_{\rm obs}| - |F_{\rm calc}|$

(*hkl*)	(024)	(104)	(110)	(116)	(214)	(300)	(330)
WS	−0.604	−0.577	−0.684	−0.178	−0.164	0	−0.005
WD	−0.080	−0.033	−0.090	−0.159	−0.082	−0.044	0.103
CS	−0.045	−0.011	−0.029	−0.029	−0.073	0.055	0.008
CD	−0.012	0.005	0.012	−0.014	−0.013	0.002	−0.006
WSN	−0.717	−0.183	−0.102	−0.794	−0.519	−0.962	−0.118
WDN	−0.683	−0.142	−0.173	−0.834	−0.533	−1.099	−0.032
GS	3.323	0.727	−0.708	2.548	−1.650	5.174	−1.775
LSF	−1.356	0.667	−0.084	−0.820	−0.171	−2.877	−0.967
Extinction factors for LSF	0.81	0.79	0.89	0.79	0.88	0.74	0.94

(*b*) $(|F_{\rm obs}| - |F_{\rm calc}|)/\sigma(F_{\rm obs})$

(*hkl*)	(024)	(104)	(110)	(116)	(214)	(300)	(330)
WSN	−2.675	−0.871	−0.785	−2.413	−2.634	−1.661	−0.593
WDN	−2.776	−0.706	−1.384	−2.799	−3.099	−2.176	−0.244
GS	0.817	0.540	−1.069	2.008	−1.349	0.896	−1.460
LSF	−4.110	1.389	−0.391	−1.413	−0.612	−1.506	−6.044

electron density of -0.03 e Å^{-3} appears at point *C*, a value that can reach $-0.30\,(5)$ e Å^{-3} depending on the refinement strategy! This result is puzzling and needs to be discussed since the electron density must be positive everywhere. One explanation is that the standard multipolar model applied to experimental data fails to describe accurately some interatomic regions owing to a series-termination effect in the multipolar expansion. In order to improve the refinements, higher multipoles were added in modelling the Al densities. The symmetry-allowed spherical harmonics up to $l = 6$ had to be included [*i.e.* three y_{lmp} functions for $l = 5$ and five y_{lmp} functions for $l = 6$ (Kurki-Suonio, 1977)]; their radial functions are given in Table 4. With these additional multipoles, the *WIEN* data

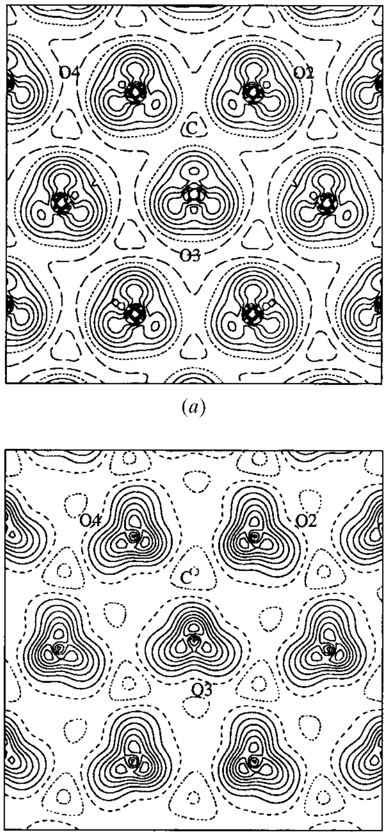

(*a*)

(*b*)

Figure 6
Static deformation density in the O_2—O_3—O_4 plane perpendicular to the *c* axis, passing only through oxygen atoms. Point *C* is the centre of the common face between two Al octahedra (see Fig. 1): (*a*) directly calculated from *WIEN97*; (*b*) obtained from *MOLLY* refinement ($l_{\max} = 4$) with WSN data. Contours as in Fig. 5.

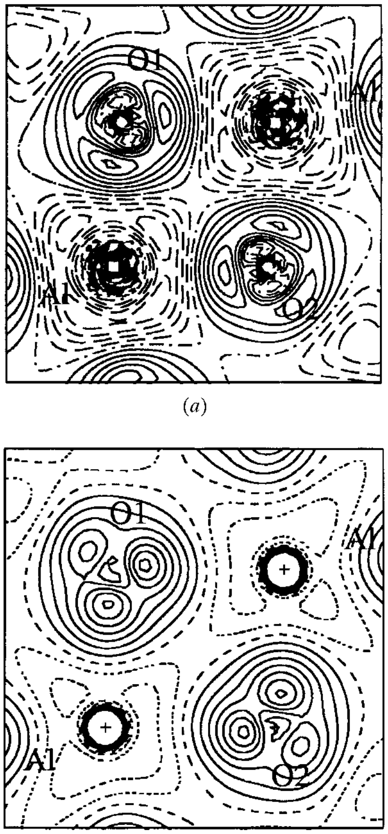

(*a*)

(*b*)

Figure 7
Static deformation density in the O_1—Al—O_2 plane passing through two Al and two O atoms and showing the two different Al—O bonds: (*a*) directly calculated from *CRYSTAL95*; (*b*) obtained from *MOLLY* refinement ($l_{\max} = 4$) with CS data. Contours as in Fig. 5.

can be fitted much better (Fig. 3*d*) and now the agreement is comparable to the *CRYSTAL* results (CS and CD) (Table 5). The differences in electron densities between $l_{\max} = 6$ and $l_{\max} = 4$ refinements, respectively, are represented in Figs. 10(*a*) and 10(*b*). The improved model affects the electron density in the following way: the main differences are situated in the vicinity of both Al and O, a positive electron density is formed (0.01 e Å^{-3}) on the oxygen atom and a negative electron density (−0.05 e Å^{-3}) centred around aluminium. As a consequence, the scale factor increased by 5σ and its standard uncertainty was halved (Table 6). Outside the nuclear regions, the maximum difference is at point *C* (+0.02 e Å^{-3}). At this point, the change in electron density is related to adding diffuse features of the higher-order multipoles ($l = 5$ and $l = 6$). For these two orders, the chosen respective Slater-type exponents, $n = 7$ and 8, correspond to maxima in the radial functions at 1.11 and 1.27 Å from the aluminium atom. Higher multipoles build up density in these interatomic regions and thus both problems, the negative electron density and the few reflections badly fitted by the model, are related to each other. The most significant evolution of parameters when adding higher multipoles for the WS data are given in Table 6: these latter parameters are within the same range as those obtained from all other data even if they significantly differ from the previous $l_{\max} = 4$ refinement. The changes in the model lead to smaller estimated uncertainties on the Al and O positions, the s.u.'s on these parameters being divided by two, because the residual $\sum w\Delta^2$ is lower. The same conclusion can be drawn for the scale factor which increased by 5σ. All the κ and κ' changed significantly considering their s.u.'s but without great differences in the electron density as discussed before (Fig. 10).

The improvement in the *WIEN* data sets is interpreted in the following way: in the *WIEN* calculations, inside the atomic spheres a partial wave expansion (numerical radial functions times spherical harmonics) is used as basis for the wavefunctions, while plane waves are used in the interstitial regions. This represents a very flexible basis set, which requires, in principle, an infinite l expansion. Usually this l expansion is truncated at $l = 10$ for the wave function, which in principle corresponds to $l = 20$ for the electron density! Therefore, one should not truncate the multipolar refinement at $l_{\max} = 4$ but expand the aluminium density at least to $l_{\max} = 6$. In the *CRYSTAL* calculations, however, $l_{\max}$ for the wavefunction is only 2 and thus order 4 is the maximum required in the density fit. It is interesting to note that this extended basis-set refinement of the electron density was also necessary for the experimental data and it decreased the problem of the negative electron density by nearly 0.05 e Å^{-3}.

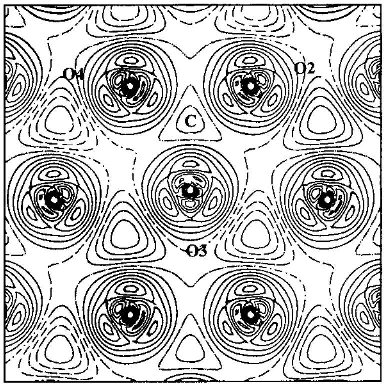

(*a*)

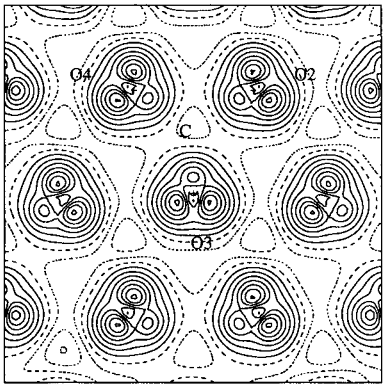

(*b*)

Figure 8
Static deformation density in the $O_2—O_3—O_4$ plane perpendicular to the *c* axis, passing only through oxygen atoms. Point *C* is the centre of the common face between two Al octahedra (see Fig. 1): (*a*) directly calculated from *CRYSTAL95*; (*b*) obtained from *MOLLY* refinement ($l_{\max} = 4$) with CS data. Contours as in Fig. 5.

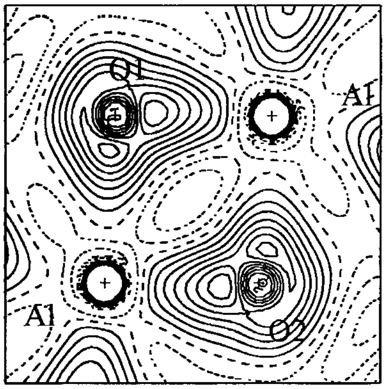

(*a*)

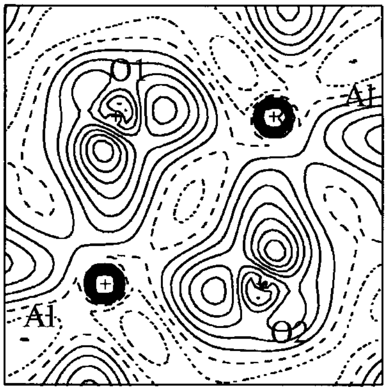

(*b*)

Figure 9
Static deformation density in the $O_1—Al—O_2$ plane passing through two Al and two O atoms and showing the two different Al—O bonds: (*a*) obtained from *MOLLY* refinement with GS data; (*b*) obtained from *MOLLY* refinement with LSF data. Contours as in Fig. 5.

5. Concluding remarks

Comparisons in direct (residual and deformation densities) and reciprocal space (difference between structure factors) were made for different data sets (theoretical and experimental), in order to judge the capability of the multipolar model to recover the electron density in corundum. We have shown that the electron densities agree within 0.1 e Å^{-3} in most cases and that a slight increase of electron density around the O atom is observed with dynamic data.

In order to properly fit the data, two improvements had to be made:

(i) A core κ parameter for Al had to be added. This significantly reduced the fitting error for all data sets, in particular for the *WIEN* data. The resulting κ core values obtained from the experimental data are hardly significant and would require higher resolution and more accurate data.

(ii) One drawback of the standard multipolar refinement to corundum was that it can lead to an electron density that is not positive everywhere. This is most important with experimental data (where extinction can cause this problem), but it was also observed with theoretical and GS data for which extinction can be excluded. The proposed solution is to increase the limit of the multipole expansion of the electron density to higher l values ($l_{\max} = 6$ is needed to fit the *WIEN* data and to avoid negative densities in the experimental maps).

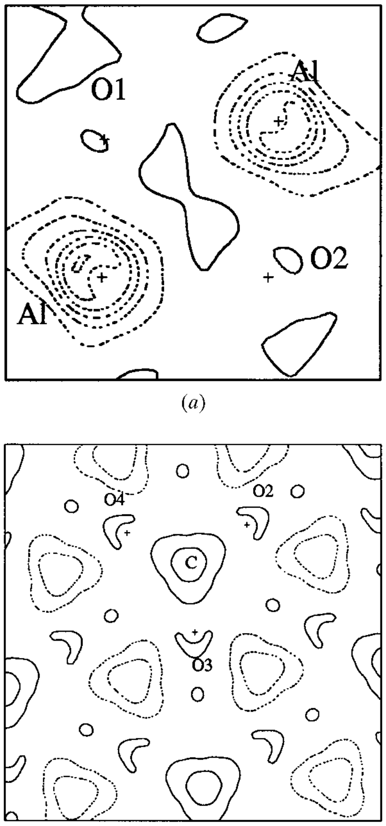

(*a*)

(*b*)

Figure 10
Difference electron density [$\Delta\rho = \rho(l_{\max} = 6) - \rho(l_{\max} = 4)$] as calculated from the two $l_{\max}$ limits for WS data; (*a*) in the $O_1—Al—O_2$ plane and (*b*) in the $O_2—O_3—O_4$ plane. Contours as in Fig. 4.

These additional multipole terms improved the agreement factors and the deformation densities, as can be seen from the corresponding residual densities. The $l = 5$ and $l = 6$ multipoles are important to better describe the density far from the atoms, as shown for example at the cage critical point *C*. One must carefully inspect the total density for being positive definite and not only the deformation density along the multipole refinements. This also demonstrates the necessity of adding a positivity constraint on the electron density during refinements.

A comparison between the densities from various experimental data sets and theoretical densities was not the scope of the present paper and will be made in a forthcoming publication. We will compare them in direct and reciprocal space as well as by means of a topological analysis.

APPENDIX *A*

In this Appendix, we describe the procedure followed to generate the sets of noisy data, starting from the calculated structure-factor amplitudes. We will focus on the set of 1632 static noisy structure factors (WSN), generated from the amplitudes computed with the *WIEN* program. All other noisy data were calculated following an equivalent procedure.

A1. Scaling and re-indexing of the data sets

First, the indices for the experimental (LSF) and theoretical (WS) structure factors were brought to a common asymmetric unit in reciprocal space, $0 \le h \le 15$, $0 \le k \le 5$, $0 \le l \le 48$. Then, the two data sets were scaled to a common normalization in order to assess reasonable values of $\sigma(F^2_{\rm WS})$; the observed structure-factor amplitudes with $F > 3\sigma(F)$ were brought onto the scale of the theoretical ones by $F^{\rm scal}_{\rm WS} = F^{\rm obs}_{\rm GS} \times {\rm scale}$.

After scaling, only two pairs of values, those for (300) and (1,2,14), were off by more than $4\sigma(F)$. Both reduction to the same asymmetric unit and scaling were performed with the program *SORTAV* (Blessing, 1989).

A2. Generation of $\sigma(F^2_{\rm WS})$

The addition of Gaussian noise to the theoretical squared amplitudes requires estimation of the uncertainties $\sigma(F^2_{\rm WS})$. With the assumption of isotropic noise in reciprocal space, a calibration curve was set up based on the experimental squared amplitudes and their associated standard uncertainties; from this curve, the values of $\sigma(F^2_{\rm WS})$ were read off. In the rest of this paragraph, we examine more closely the steps leading to the estimation of $\sigma(F^2_{\rm WS})$. A set of values for the square of the amplitudes, $F^2_{\rm LSF}$, and the associated uncertainties, $\sigma(F^2_{\rm LSF})$, have been computed using the computer program *BAYES* (Blessing, 1989), based on the previously scaled experimental structure-factor amplitudes. Fig. 11 reports the values of $\ln\sigma(F^2_{\rm LSF})$ *versus* $\ln(F^2_{\rm LSF})$. The data were then averaged in bins and a cubic interpolation spline fitted to them (an extra point corresponding to $F^2_{\rm LSF} = 10^{-6}$, $\sigma(F^2_{\rm LSF}) = 10^{-5}$, has been added to allow interpolation of very small theoretical squared structure amplitudes). Fig. 12 reports the values of $\ln\sigma(F^2_{\rm WS})$ obtained by the interpolating spline from the values of $\ln F^2_{\rm WS}$. Obviously, the spline interpolation to estimate the s.u.'s for the weakest reflections is less than satisfactory; a constant value for these s.u.'s would have given a more physical value of $\sigma(F^2_{\rm WS})$ for these data.

A3. Generation of the noise

Gaussian noise that is proportional to the associated s.u.'s has been added onto the 1632 theoretical squared amplitudes:

$$|F_{\rm WSN}|^2 = |F_{\rm WS}|^2 + {\rm Gauss} \times \sigma(|F_{\rm WS}|^2), \qquad (7)$$

where Gauss is a random deviate of zero mean and unit variance. After this step, 55 reflections had squared amplitudes less than zero. The values for the amplitudes $|F_{\rm WSN}|$ and the associated uncertainties $\sigma(F_{\rm WSN})$ were computed using the computer program *BAYES* (Blessing, 1989) based on the previously obtained noisy squared structure amplitudes.

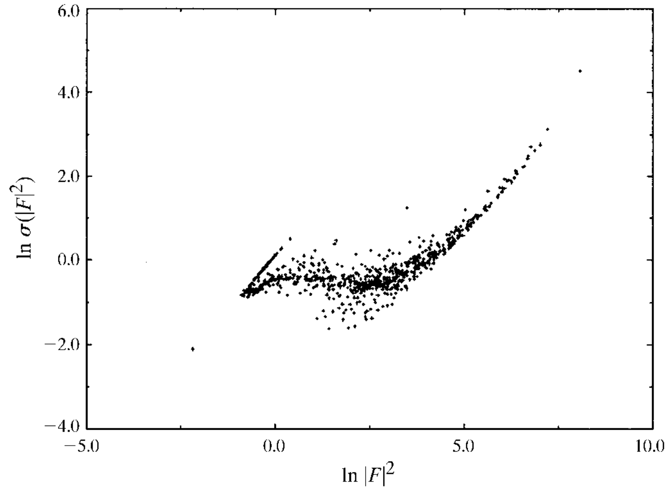

Figure 11
Plot of $\ln\sigma(|F|^2_{\rm obs})$ *versus* $\ln|F|^2_{\rm obs}$ for the 802 experimental squared structure amplitudes of LSF.

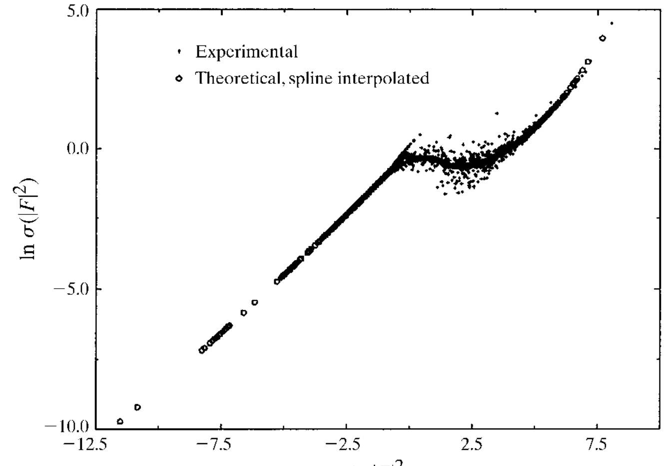

Figure 12
Plot of $\ln\sigma(|F|^2_{\rm th})$ *versus* $\ln|F|^2_{\rm th}$ from the spline interpolation of the values plotted in Fig 11.

We would like to thank Professor D. Schwarzenbach for providing us with the experimental corundum data set (LSF). Professor N. K. Hansen is also gratefully acknowledged for help in the $l = 5$ and $l = 6$ spherical harmonics calculation routine.

References

Abramov, Y. A., Volkov, A. V. & Coppens, P. (1999). *Chem. Phys. Lett.* **311**, 81–86.

Azavant, P., Lichanot, A., Rérat, M. & Chaillet, M. (1994). *Theor. Chim. Acta*, **89**, 213–226.

Azavant, P., Lichanot, A., Rérat, M. & Pisani, C. (1996). *Int. J. Quantum Chem.* **58**, 419–429.

Becker, P. J. & Coppens, P. (1974). *Acta Cryst.* A**30**, 129–153.

Becker, P. J. & Coppens, P. (1975). *Acta Cryst.* A**31**, 417–425.

Blaha, P., Schwarz, K. & Luitz, J. (1997). *WIEN97*. Technical University Vienna. Improved and updated Unix version of the original copyright *WIEN* code.

Blaha, P., Schwarz, K., Sorantin, P. & Trickey, S. B. (1997). *Comput. Phys. Commun.* **59**, 399.

Blessing, R. H. (1989). *J. Appl. Cryst.* **22**, 396–397.

Brown, A. S., Spackman, M. A. & Hill, R. J. (1993). *Acta Cryst.* A**49**, 513–527.

Clementi, E. & Roetti, C. (1974). *At. Data Nucl. Data Tables*, **14**, 177–478.

Coppens, P. (1967). *Science*, **158**, 1577.

Coppens, P., Abramov, Y., Carducci, M., Korjov, B., Novozhilova, I., Alhambra, C. & Pressprich, M. R. (1999). *J. Am. Chem. Soc.* **121**, 2585–2593.

Coppens, P., Guru Row, T. N., Leung, P., Stevens, E. D., Becker, P. J. & Yang, Y. W. (1979). *Acta Cryst.* A**35**, 63–72.

Dovesi, R., Saunders, V. R., Roetti, C., Causà, M., Harrison, N., Orlando, R. & Aprà, E. (1996). *CRYSTAL95 Users Manual*. Theoretical Chemistry Group of Torino, Italy, and CCLRC Daresbury Laboratory, England.

Epstein, J., Bentley, J. & Stewart, R. F. (1977). *J. Chem. Phys.* **66**, 5564–5567.

Graafsma, H., Souhassou, M., Puig-Molina, A., Harkema, S., Kvick, A. & Lecomte, C. (1998). *Acta Cryst.* B**54**, 193–195.

Hansen, N. K. & Coppens, P. (1978). *Acta Cryst.* A**34**, 909–921.

Iversen, B. B., Larsen, F. K., Figgis, B. N. & Reynolds, P. A. (1997). *J. Chem. Soc. Dalton Trans.* pp. 2227–2240.

Kirfel, A. & Eichhorn, K. (1990). *Acta Cryst.* A**46**, 271–284.

Koritzansky, T., Howard, S., Mallison, P. R., Su, Z., Richter, T. & Hansen, N. K., (1995). *XD*, a computer program package for multipole refinement and analysis of charge densities from diffraction data. Institute for Crystallography, Berlin, Germany.

Kurki-Suonio, K. (1977). *Isr. J. Chem.* **16**, 115–123.

Lewis, J., Schwarzenbach, D. & Flack, H. J. (1982). *Acta Cryst.* A**38**, 733–739.

Maslen, E. N., Streltsov, V. A., Streltsova, N. R., Ishizawa, N. & Satow, Y. (1993). *Acta Cryst.* B**49**, 973–980.

Moss, R. G., Souhassou, M., Blessing, R. H., Espinosa, E. & Lecomte, C. (1995). *Acta Cryst.* B**51**, 650–660.

Perdew, J. P., Burke, K. & Ernzerhof, M. (1996). *Phys. Rev. Lett.* p. 3865.

Perdew, J. P., Burke, K. & Ernzerhof, M. (1997). *Phys. Rev. Lett.* p. 1396.

Pérès, N., Boukhris, A., Souhassou, M., Gavoille, G. & Lecomte, C. (1999). *Acta Cryst.* A**55**, 1038–1048.

Salasco, L., Dovesi, R., Orlando, R., Causà, M. & Saunders, V. R. (1991). *Mol. Phys.* **72**, 267–277.

Souhassou, M., Espinosa, E., Lecomte, C. & Blessing, R. H. (1995). *Acta Cryst.* B**51**, 661–668.

Souhassou, M., Pillet, S. & Hansen, N. K. (1999). Internal report. Laboratoire de Cristallographie et Modélisation des Matériaux Minéraux et Biologiques, Université Henri Poincaré, Nancy I, France.

Spackman, M. A., Byrom, P. G., Alfredsson, M. & Hermansson, K. (1999). *Acta Cryst.* A**55**, 30–47.

Stewart, R. F. (1969). *J. Chem. Phys.* **51**, 4569–4577.

Stewart, R. F. (1979). *Chem. Phys. Lett.* **65**, 335–342.

Stewart, R. F. & Spackman, M. A. (1981). *VALRAY Users Manual.* Preliminary Draft. Department of Chemistry, Carnegie–Mellon University, Pittsburg, PA 15213, USA.

Zavodnik, V., Stash, A., Tsirelson, V., de Vries, R. & Feil, D. (1999). *Acta Cryst.* B**55**, 45–54.

Zuo, J. M., Blaha, P. & Schwarz, K. (1997). *J. Phys. Condensed Matter*, **9**, 7541–7561.